

Supplementary Materials for

Room-temperature ferromagnetism at an oxide/nitride interface

Qiao Jin, Zhiwen Wang, Qinghua Zhang, Yonghong Yu, Shan Lin, Shengru Chen, Mingqun Qi, He Bai, Amanda Huon, Qian Li, Le Wang, Xinmao Yin, Chi Sin Tang, Andrew T. S. Wee, Fanqi Meng, Jiali Zhao, Jia-Ou Wang, Haizhong Guo, Chen Ge, Can Wang, Wensheng Yan, Tao Zhu, Lin Gu, Scott A. Chambers, Sujit Das, Timothy Charlton, Michael R. Fitzsimmons, Gang-Qin Liu, Shanmin Wang, Kui-juan Jin,* Hongxin Yang,* and Er-Jia Guo*

* Corresponding author. Emails: kjjin@iphy.ac.cn; hongxin.yang@nimte.ac.cn; and ejguo@iphy.ac.cn

Experimental section

Synthesis of CrN/Cr₂O₃ superlattices. The CrN/Cr₂O₃ superlattices were fabricated by plasma-assisted pulsed laser deposition with two ceramic targets, CrN and Cr₂O₃. The Cr₂O₃ target was fashioned from commercial powder and sintered at 1000 °C for 6 hours. The CrN target was synthesized using a high-pressure reaction route from a mixture of CrCl₃ and NaNH₂ powders. The mixed powder was sintered as a ceramic polycrystalline target at 5 GPa and 1000°C for an hour. Superlattices were deposited by alternatively ablating the two stoichiometric targets. The interlayer thickness was controlled by counting the number of laser pulses and was confirmed by x-ray reflectometry. The thickness of the individual CrN and Cr₂O₃ layers was varied from approximately 0.5 to 5 nm and the CrN/Cr₂O₃ bilayer was repeated ten times. Before thin-film deposition, the Al₂O₃ substrates (Hefei Kejing Mater. Tech. Co., LTD) were pre-annealed at 1000 °C to achieve atomically flat surfaces with step-terrace morphology. We initiated each superlattice with a CrN layer and ended with a Cr₂O₃ layer to prevent the CrN top layer from oxidation. The growth temperature, laser fluence, and repetition rate for all layers were 600°C, ~1.5 J/cm², and 3 Hz, respectively. During the deposition of CrN layers, atomic nitrogen was generated using an RF plasma source (Oxford Applied, Co., LTD). The RF power was kept at 250 W and the nitrogen flow was maintained 1.5 sccm/min. Optimized growth conditions ensure that the as-grown CrN films is nearly stoichiometric and exhibit its intrinsic physical properties. The plasma source was shuttered during the growth of Cr₂O₃ layers. Following deposition, all superlattices were cooled slowly at a rate of -5°C/min to room temperature. To eliminate the influence of interfacial mixing on the magnetic properties, we fabricated a CrN film with a thickness of 20 nm in the oxygen partial pressure of 0.1 Torr and a Cr₂O₃ film with a thickness of 20 nm under the N-plasma. Additionally, we deposited a CrN-Cr₂O₃ alloy film by pulsed laser deposition. The experimental conditions were kept the same as those for growing the CrN/Cr₂O₃ superlattices. Laser ablation was alternated randomly between CrN and Cr₂O₃ sintered targets. The numbers of laser pulses on each target are less than the pulse numbers that are required for growing a single unit cell of CrN and Cr₂O₃. Thin films grown in this manner are completely mixed as an alloy.

Structural characterization and elemental mapping. The crystalline quality of all superlattices was determined by synchrotron x-ray diffraction (sXRD) at beamlines 1W1A of

the Beijing Synchrotron Radiation Facility (BSRF) and 02U2 of the Shanghai Synchrotron Radiation Facility (SSRF). The morphologies of the substrates and superlattices were characterized with an Asylum MFP-3D in tapping mode at ambient conditions. Cross-sectional TEM specimens were prepared using a standard focused ion beam (FIB) lift-off process along the $[10\bar{1}0]$ orientation and examined using a JEM ARM 200CF microscope at the Institute of Physics, Chinese Academy of Sciences. Atomic-resolved HAADF images were collected with a convergence angle of 28.5 mrad and a collection angle of 90 – 370 mrad. Electron-energy-loss-spectroscopy (EELS) mapping was performed at the N K -, O K -, and Cr L -edges, respectively, and the EELS signals were appropriately integrated after background subtracting. All STEM data were analyzed using Gatan DigitalMicrograph.

Physical properties characterization. The magnetic properties of the superlattices were measured using a MPMS3 (Quantum Design). The magnetic hysteresis loop at each temperature of interest was obtained up to ± 5 T, after subtracting a linear background to correct for the diamagnetic response from the substrates. The M - T curves were measured after zero-field or field-cooling at 1 kOe. The transport measurements were performed in a van der Pauw configuration using a PPMS (Quatum Design). The current was kept constant at 100 μ A for all electrical measurements. The contacts were prepared using wire-bonding to ensure that all interfaces were electrically well connected.

Spectroscopic measurements. X-ray absorption measurements were conducted at beamline 4B9B of the Beijing Synchrotron Radiation Facility (BSRF) at ambient temperature. X-ray magnetic circular dichroism was measured at beamline SINS of the Singapore Synchrotron Light Source (SSLS) and the XMCD beamline at the National Synchrotron Radiation Laboratory (NSRL) in China. All XAS and XMCD measurements were conducted in total electron yield (TEY) mode at an angle of incidence of $\sim 30^\circ$ off the sample surface plane. All XAS were measured at ambient temperature. Temperature dependent XMCD was averaged from multiple measurements at magnetic fields of ± 0.7 T applied parallel to the film plane to correct the possible nonmagnetic artifacts. All spectra were normalized to their pre- and post-edges using a step function to facilitate direct comparison. Room-temperature XPS measurements were performed at Pacific Northwest National Laboratory. Spectra were collected at different electron emission angles in order to obtain the different photoelectron

probe depths.

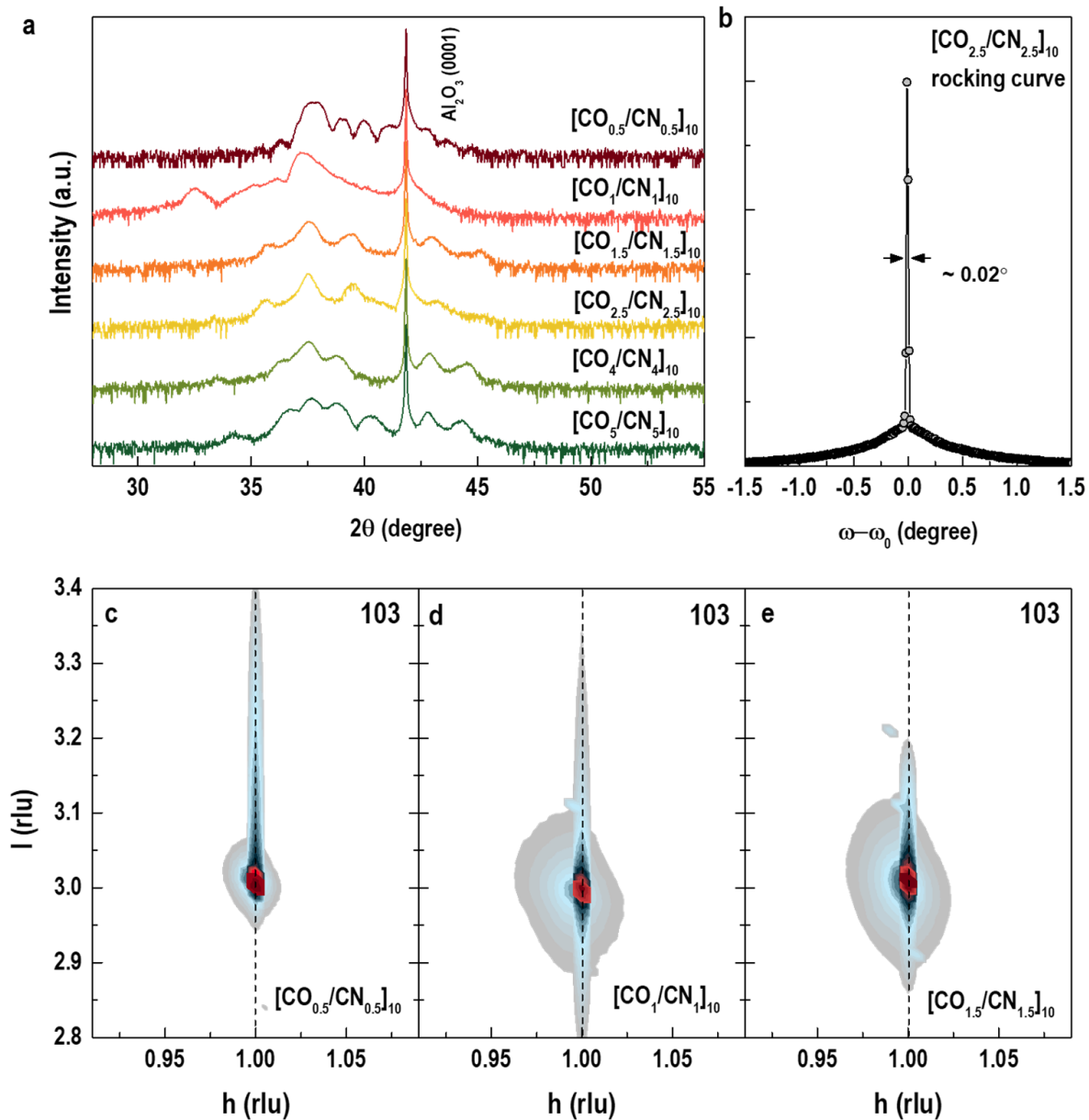
Nanoscale magnetization profiling using PNR. We performed PNR measurements on a $[\text{CO}_{0.5}/\text{CN}_{0.5}]_{10}$ superlattice at the multipurpose reflectometer (MR) beamline of the Chinese Spallation Neutron Source (CSNS), Chinese Academy of Sciences (CAS) and Magnetic Reflectometer (BL-4A) beamline of the Spallation Neutron Source (SNS), Oak Ridge National Laboratory (ORNL). At the CSNS-CAS, the sample was field-cooled and measured with an in-plane magnetic field of 1 T at 10 K. At the SNS-ORNL, the identical sample was re-measured with an in-plane magnetic field of 4.8 T at 10 K. The reflected spin-up (R^{++}) and spin-down (R^{--}) neutrons were collected in the specular reflection geometry with the wave vector transfer (\vec{q}) perpendicular to the sample surface plane. We plotted the specular reflectivities as a function of \vec{q} ($= 4\pi\sin\theta/\lambda$), where θ is the neutron incident angle and λ is the neutron wavelength. The spin-asymmetry (SA) was calculated by $(R^{++}-R^{--})/(R^{++}+R^{--})$. PNR data fitting was performed using the GenX program as well as Ref1D code. The chemical depth profiles of superlattices were constrained to the models obtained by fitting x-ray reflectivities. We fitted the PNR data to the models with separated magnetization model and uniform magnetization model. The magnetization of CrN and Cr_2O_3 interlayers were then deduced. The high-quality \vec{q} data ensure the certainty, as indicated by figure of merit value (\times), of small magnetic moments obtained from PNR fittings.

Diamond NV-based magnetometry. The diamond NV-based magnetometry measurements were carried out using a home-built optically detected magnetic resonance (ODMR) system. The temperature of the sample was controlled and monitored using conventional thermometer attached on the sample stage. The maximum stable temperature is the ambient temperature. Nanodiamonds (NDs) with a nominal diameter of 100 nm and typically ~ 500 NV centers per crystal were used (Adámas Nanotechnologies). We dispersed the NDs on the superlattice surface randomly with a low density so that individual NDs could be addressed and probed with the confocal microscope (Fig. S9a). ODMR spectra were taken by sweeping the microwave frequency through resonance and recording the photon counts as the laser excitation was always on. The ground states of NV center are spin-1 and there is only one resonant dip at 2870 MHz at zero magnetic field ($m_s = \pm 1$ states are degenerated). If a stray field is generated by the SL sample, the ODMR spectrum of an NV center will split into two dips due

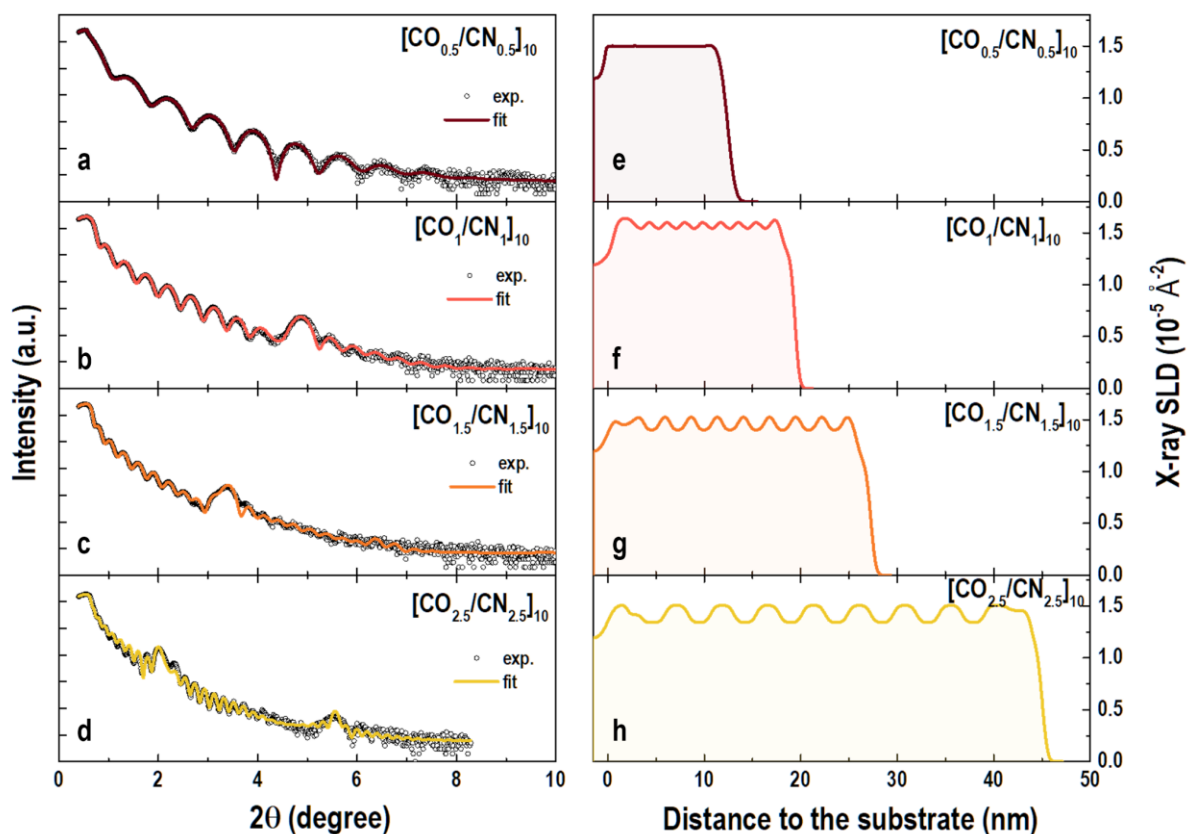
to the Zeeman effect. The splitting is proportion to the strength of the stray field. Please note that there are hundreds of NV centers in a single ND and the stray field may have a gradient at the 100-nm scale, so the ODMR spectra of NDs on SLs are broadened as compared to that of a single NV center. We measured ODMR spectra of more than 20 NDs at two fix temperatures, 89 K and 300 K (Fig. S9a and up pane of Fig. S9b). Typical temperature dependent ODMR spectra are shown in Fig. 3B of the main text. For some NDs, their local stray field was so large that the two-peak feature of the ODMR spectra were disappeared. Under these circumstances, we extracted the local field strength from the width of single-peak Lorentz fitting, which also presented clear temperature dependence, as shown in Fig. S9 (c-e). These results indicate that the superlattices exhibit a higher magnetic net moment at 89 K than that at 295 K. As a comparison, we also measured ODMR spectra of NDs on a bare Al₂O₃ substrate. Nearly no temperature dependence was observed on a bare Al₂O₃ substrate (Fig. S9b, bottom pane). This comparison indicates that the magnetic signals from NV-center magnetometry is originated from the SL sample.

DFT calculations. First-principles calculations were performed within the framework of density functional theory (DFT) implemented in VASP. The projected augmented wave (PAW) method was used to describe ion core-electron interactions and exchange correlation effects were treated by the generalized gradient approximation (GGA) in the form of Perdew–Burke–Ernzerhof (PBE) functional. The cutoff energy for plane-wave expansion was set to 520 eV and the Brillouin zone (BZ) was meshed by the $7\times 7\times 4$, $7\times 7\times 3$ and $7\times 7\times 2$ Monkhorst–Pack grids for Cr₂O₃/CrN superlattices with layer thicknesses ranging from 2 to 4 u.c., respectively. To describe the strong on-site Coulomb interaction (U) caused by the localized $3d$ electrons in Cr, the GGA+ U approximation was employed with an effective U value of 3.5 eV. All calculation parameters are carefully checked to ensure the total energy of the superlattices converged below 10^{-7} eV. Atomic positions were fully relaxed with the force acting on each atom being less than 0.001 eV/Å. The optimized unit cell parameters for the CrN ($a = 5.98$ Å, $b = 2.98$ Å, $c = 4.15$ Å) and Cr₂O₃ ($a = b = 5.05$ Å, $c = 13.82$ Å) were chosen as starting points to create the theoretical model for the superlattices. According to the STEM-HHADDF results, the CrN and Cr₂O₃ layers in the superlattices were modeled along the (111) and (001) crystallographic orientations, respectively, due to minimization of the in-plane lattice mismatch

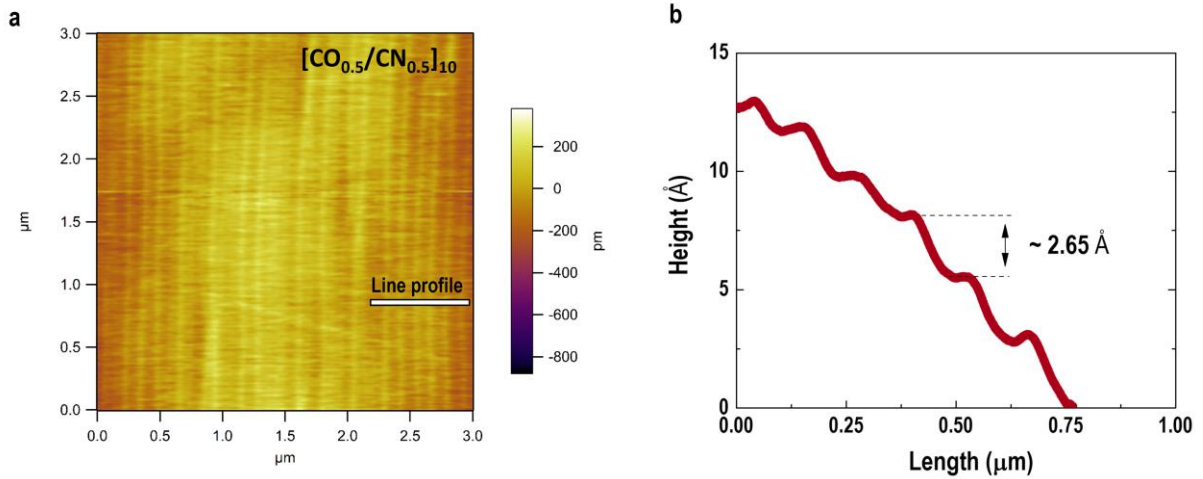
of $\sim 2.49\%$. We constructed two stacking types for the superlattices to investigate interface termination effects on the robustness of the ferromagnetism. One type of interface structure has a N termination and the other presents a O termination.



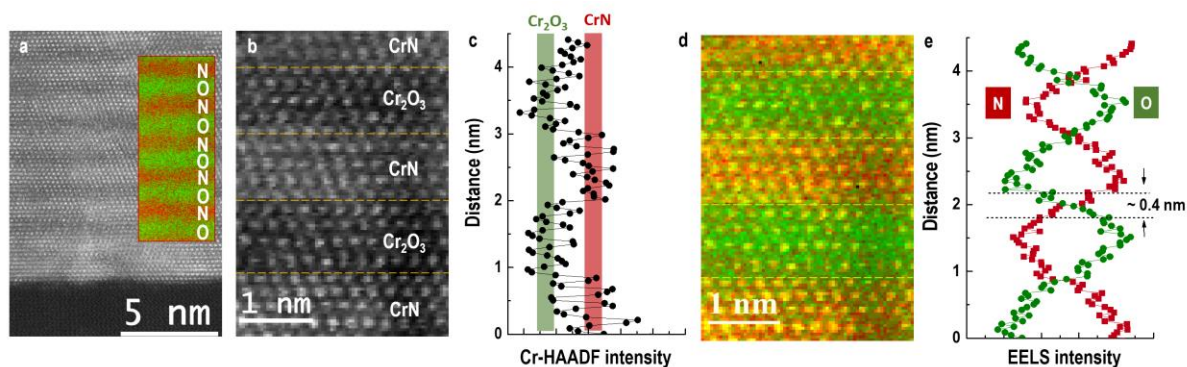
Supplementary Fig. S1. Structure characterizations of $[\text{CO}_t/\text{CN}_t]_{10}$ superlattices. (a) X-ray diffraction (XRD) θ - 2θ scans for $[\text{CO}_t/\text{CN}_t]_{10}$ superlattices, where $t = 0.5, 1, 1.5, 2.5, 4,$ and 5 nm, grown on the (0001)-oriented Al_2O_3 substrates. Distinct Laue thickness fringes near the film and SL Bragg peaks, up to three orders from the bilayer repeats, are observed. (b) Rocking curve around the SL main reflection. The FWHM is $\sim 0.02^\circ$ which is close to the FWHM of the Al_2O_3 substrate. (c)-(e) Reciprocal space maps (RSMs) around the substrates' pseudocubic 103 reflections for $[\text{CO}_{0.5}/\text{CN}_{0.5}]_{10}$, $[\text{CO}_1/\text{CN}_1]_{10}$, and $[\text{CO}_{1.5}/\text{CN}_{1.5}]_{10}$ superlattices, respectively. The RSM results indicate that all layers are coherently strained to the Al_2O_3 substrates. The sXRD measurements confirm that all superlattices are of high structural quality.



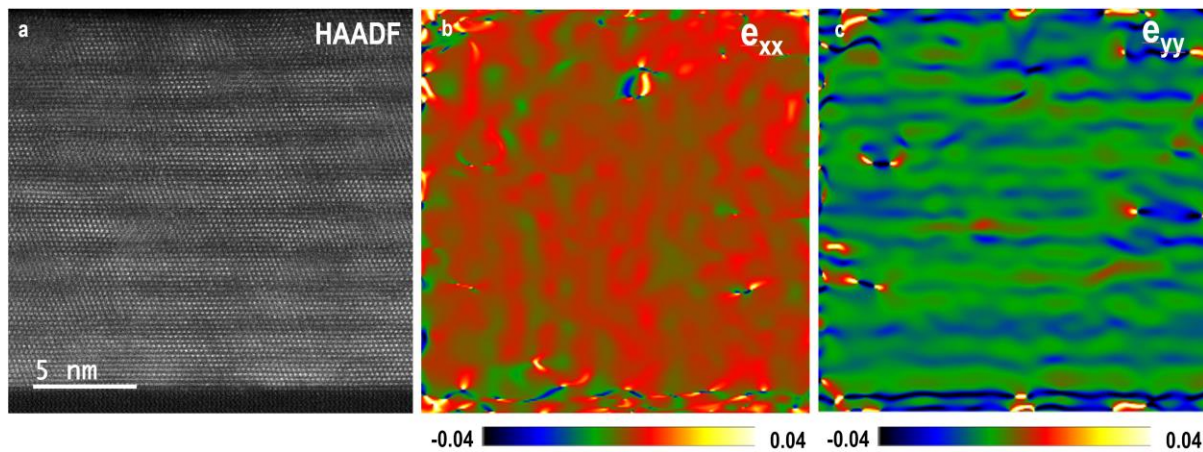
Supplementary Fig. S2. X-ray reflectivities of $[\text{CO}_t/\text{CN}_t]_{10}$ superlattices. (a)-(d) X-ray reflectivities for $[\text{CO}_t/\text{CN}_t]_{10}$ superlattices with $t = 0.5, 1, 1.5,$ and 2.5 nm, respectively. The open circles and solid lines are the experimental data and best fits, respectively. XRR data were fitted using GenX software [S1]. We obtained the x-ray scattering length densities (SLD), i. e. chemical distribution depth profiles of $[\text{CO}_t/\text{CN}_t]_{10}$ superlattices for $t = 0.5$ (e), 1 (f), 1.5 (g), and 2.5 (h). The surface and interface roughnesses for all superlattices are 4 ± 1.7 Å. X-ray SLD for the top Cr_2O_3 layer is slightly lower than that of the Cr_2O_3 layers in the film bulk, suggesting that the stoichiometry of surface layer may be changed due to the different boundary conditions. These models constrain the chemical depth profiles that were used to fit the neutron reflectivity.



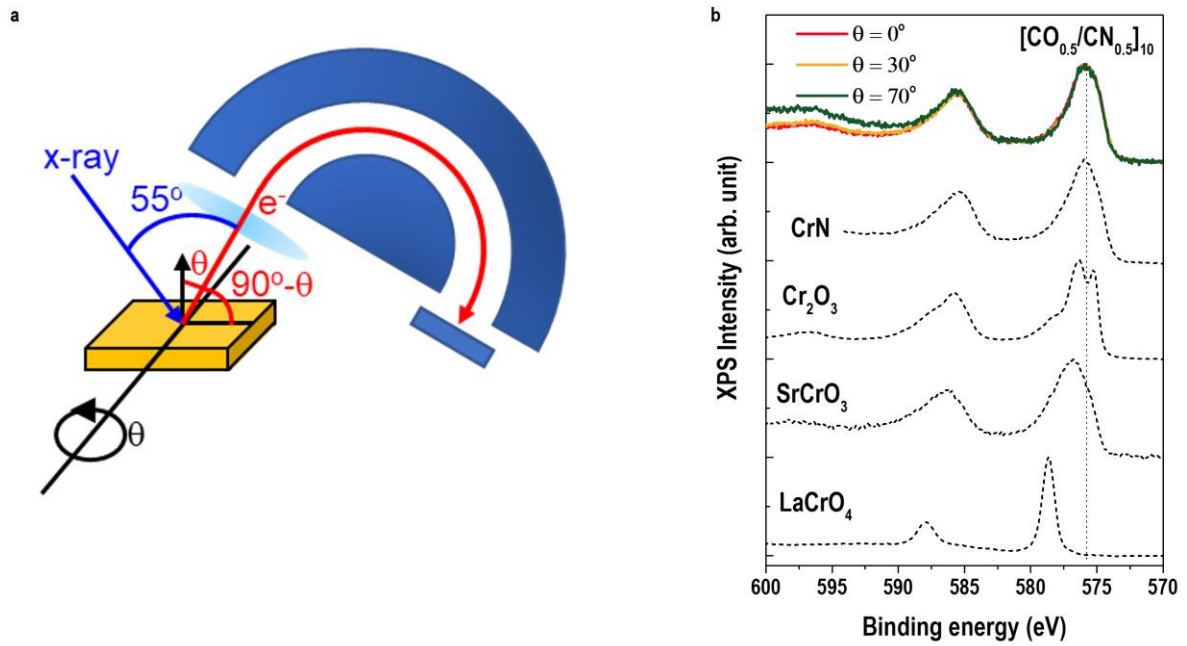
Supplementary Fig. S3. Topography of a $[\text{CO}_{0.5}/\text{CN}_{0.5}]_{10}$ superlattice. Atomic force microscopy (AFM) image recorded over an area of $3 \times 3 \mu\text{m}^2$. The measurements were repeated at different locations. A step-terrace structure was observed in all AFM images with an average RMS roughness of $\sim 3 \text{ \AA}$, revealing an atomically smooth surface. (a) A typical AFM image from a $[\text{CO}_{0.5}/\text{CN}_{0.5}]_{10}$ superlattice. A line profile across the steps is plotted in (b). The step height is approximately one unit cell thick ($\sim 2.65 \text{ \AA}$) and the step width is about $\sim 250 \text{ nm}$. The AFM results reveal that the SLs grow in step-flow mode, giving rise to atomically smooth film surfaces.



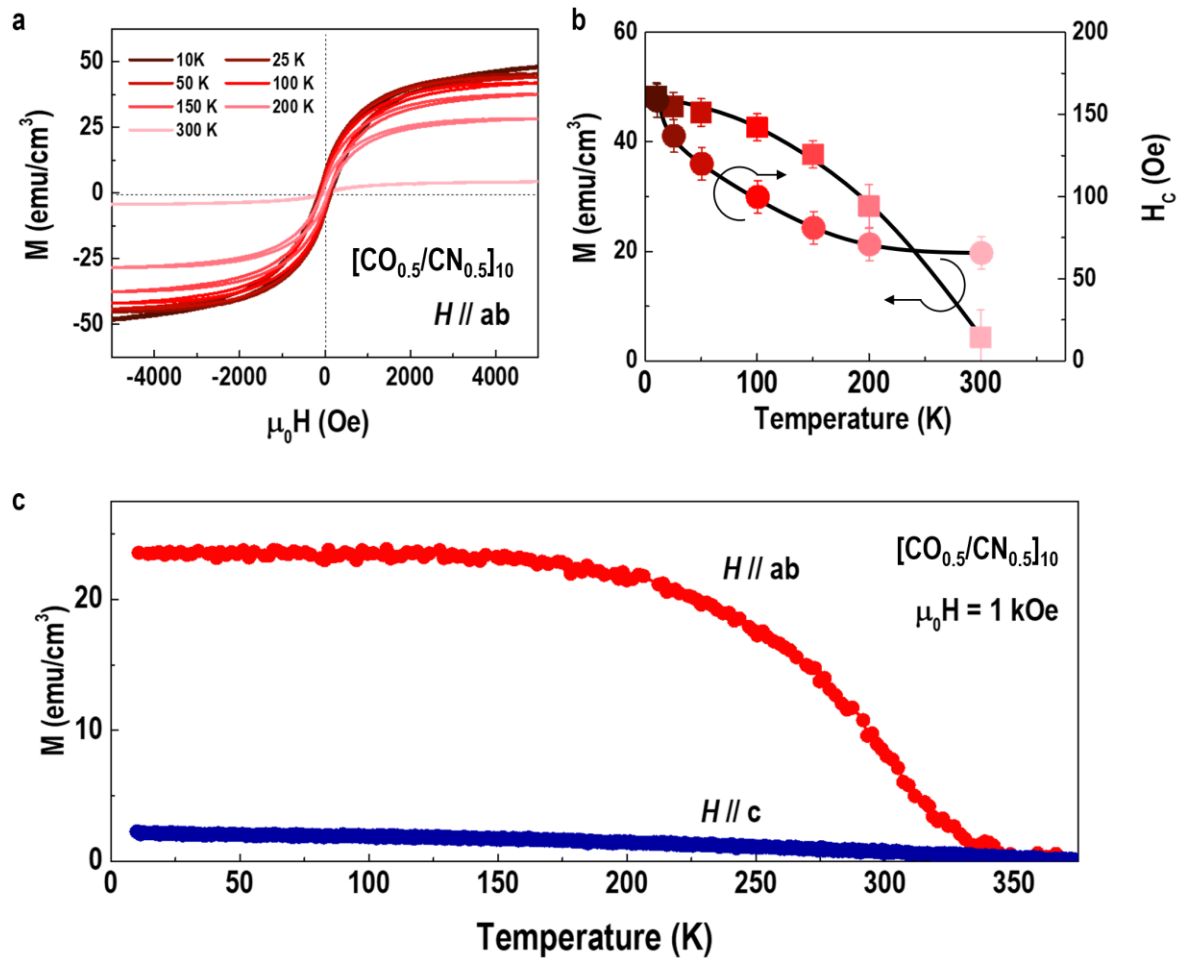
Supplementary Fig. S4. Atomic resolution STEM-EELS analysis of a $[\text{CO}_1/\text{CN}_1]_{10}$ superlattice. (a) HAADF-STEM image of a $[\text{CO}_1/\text{CN}_1]_{10}$ superlattice. (b) High-magnified HAADF image of a representative region. The bright and dark regions reveal the CrN and Cr_2O_3 layers, respectively. From the Cr-HAADF intensity profile shown in (c), we could clearly identify the CrN and Cr_2O_3 layers from the high and low intensity contrast, respectively. The contrast is due to the difference in Cr atom density along the STEM projective direction. The inset shows the EELS map in the same region. The red and green colors represent the integrated EELS signals from N K - and O K -edges, respectively. (d) and (e) show an associated EELS map and EELS profiles of O and N elements from a small portion of a $[\text{CO}_1/\text{CN}_1]_{10}$ superlattice, respectively. The Cr atoms align well crystallographically across the various CrN/ Cr_2O_3 interfaces. The EELS maps reveal that the elemental distribution within each interlayer is uniform and the CrN/ Cr_2O_3 interface is sharp with minimal chemical intermixing. From the EELS profiles, we could identify that the upper limit of chemical intermixing is approximately ~ 0.4 nm, considering the positions of 1/3 of the EELS intensities of N or O elements.



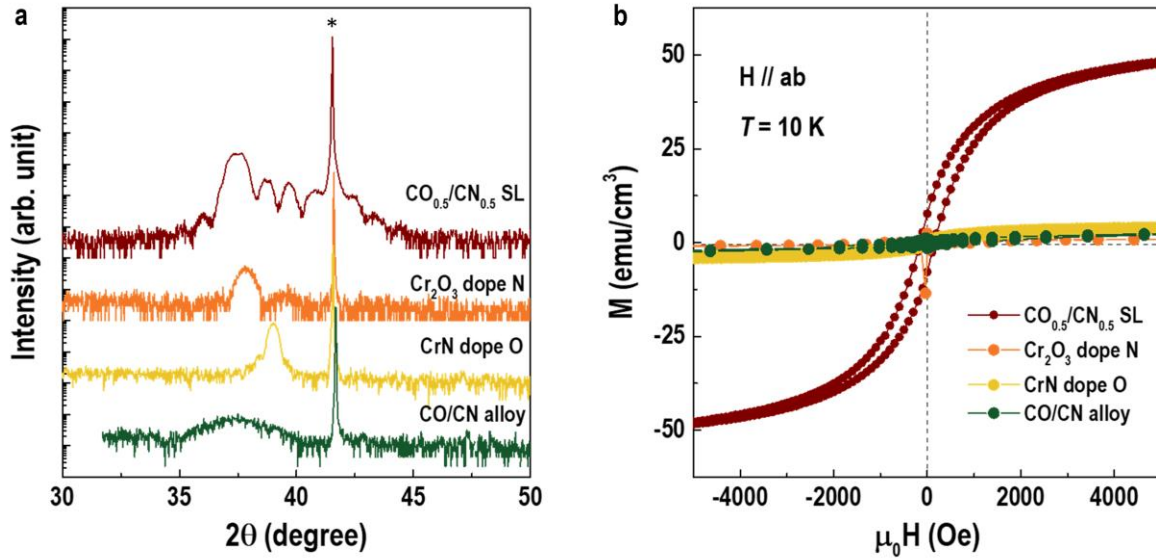
Supplementary Fig. S5. Strain analysis of a $[\text{CO}_1/\text{CN}_1]_{10}$ superlattice. We performed geometric phase analysis (GPA) of (a) the cross-sectional STEM-HAADF image. (b) and (c) show the in-plane and out-of-plane strain distributions within the superlattice, respectively. The GPA results reveal a uniform in-plane lattice constant within both CrN and Cr₂O₃ interlayers. These results are consistent with the RSM results, indicating SL coherence with the substrates. We observe a periodic modulation of the out-of-plane lattice constants along the film growth direction, as expected because the lattice constants of the individual CrN and Cr₂O₃ layers are different. From the XRD, we can only measure the volume-averaged lattice constant for the CrN/Cr₂O₃ bilayer. The estimated out-of-plane lattice constant from GPA analysis is in good agreement with that obtained from the XRD, suggesting that both methods yield robust strain analyses.



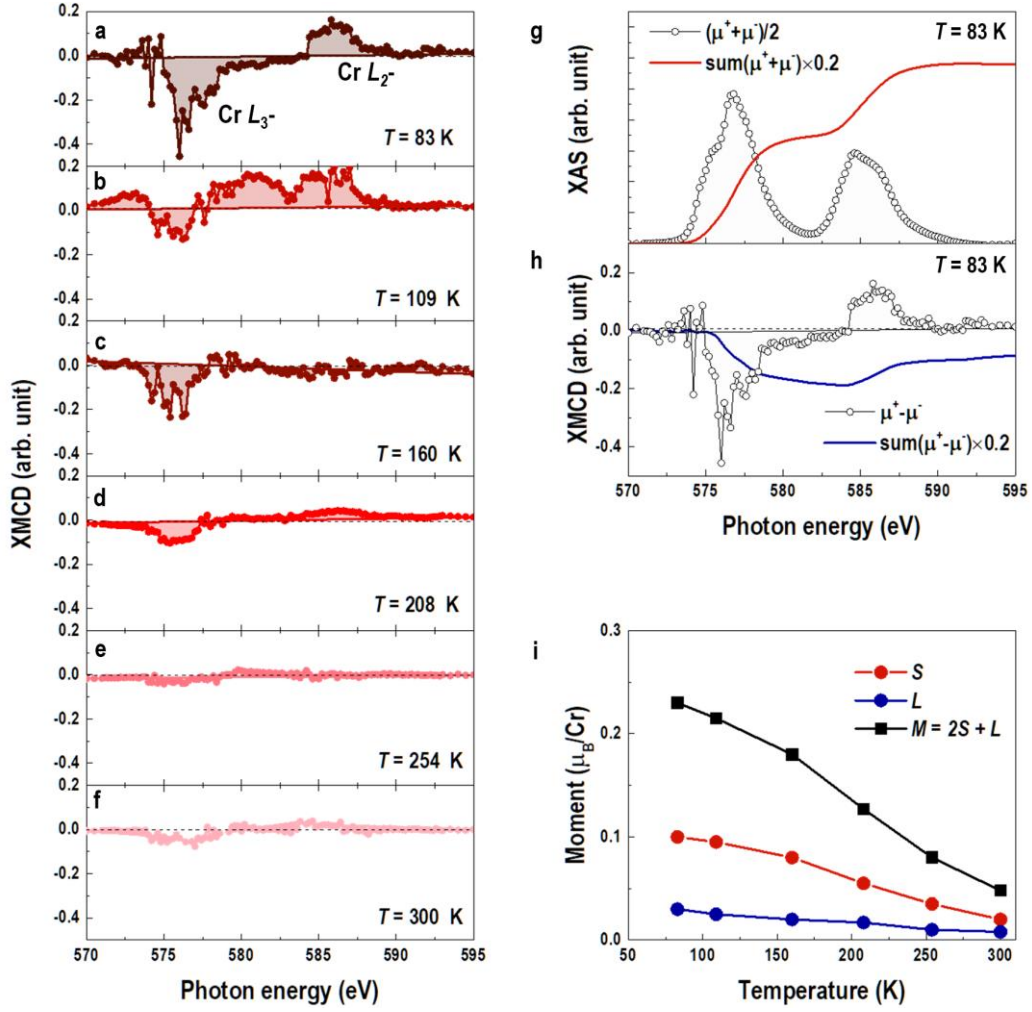
Supplementary Fig. S6. X-ray photoelectron spectra (XPS) measurements on a $[\text{CO}_{0.5}/\text{CN}_{0.5}]_{10}$ superlattice. (a) Schematic of the measurement. Monochromatic Al $K\alpha$ x-rays are incident on the SL surface at an angle of 55° with respect to the lens axis of the spectrometer. Photoelectrons are collected at an angle θ with respect to the surface normal. By increasing θ , the photoelectron probe depth can be reduced by a factor of $1/\cos(\theta)$. (b) Cr 2p core-level XPS of a $[\text{CO}_{0.5}/\text{CN}_{0.5}]_{10}$ superlattice. The dashed gray line denotes the Cr 2p binding energy for Cr^{3+}N and $\text{Cr}^{3+}_2\text{O}_3$ thin films, indicating that the valence of Cr ions in the superlattices is +3. The reference spectra for Cr^{4+} and Cr^{5+} were measured using SrCrO_3 [S2] and LaCrO_4 [S3] single crystals.



Supplementary Fig. S7. Magnetic characterizations of a $[\text{CO}_{0.5}/\text{CN}_{0.5}]_{10}$ superlattice. (a) M - H hysteresis loops measured at various temperatures with the magnetic field applied along the surface plane. (b) Temperature dependent magnetization (M at 5 kOe) (square symbols) and coercive field (H_c) (circle symbols). We observe that both M and H_c drop with increasing temperature, revealing typical ferromagnetic behavior. (c) M - T curves measured with magnetic field applied along the in-plane (red) and out-of-plane (blue) directions. The measurements were carried out during warm-up after field-cooling at 1 kOe. Apparently, the magnetic easy axis of the superlattice is along the in-plane direction, which is typical for two-dimensional superlattices composed of the ultrathin interlayers [S4-S7]. The Curie temperature of the superlattice is ~ 325 K, which is well above room temperature, illustrating a strong exchange coupling between Cr ions across the interfaces.



Supplementary Fig. S8. Structural and magnetic characterizations of a $[\text{CO}_{0.5}/\text{CN}_{0.5}]_{10}$ superlattice, an O-doped CrN film, a N-doped Cr_2O_3 film, and an intermixed alloy sample. (a) Comparison of XRD θ - 2θ scans for different samples. Apparently, all samples are highly crystallized, except for the alloy sample does not show a significant textured diffraction pattern. “*” indicates the positions of the Al_2O_3 substrates. The out-of-plane lattice constant of a N doped Cr_2O_3 film is larger than that of a O doped CrN film. After the chemical doping, the lattice constants of these films are different from those of undoped single films. [S8, S9] (b) Field-dependent magnetization for different samples. All measurements were performed after field cooling at 10 K. Magnetic measurements were taken with the magnetic fields applied along the in-plane direction. Except for the $[\text{CO}_{0.5}/\text{CN}_{0.5}]_{10}$ superlattice, the O-doped CrN film, N-doped Cr_2O_3 film, and the intermixed alloy sample exhibit nearly negligible moment and no hysteresis. These results clearly exclude the influence of interfacial intermixing, otherwise these samples should have a comparable saturation magnetization similar to that of the $[\text{CO}_{0.5}/\text{CN}_{0.5}]_{10}$ superlattice.



Supplementary Fig. S9. Temperature dependent XMCD of a [CO_{0.5}/CN_{0.5}]₁₀ superlattice. The XMCD spectra were calculated from the difference between μ^+ and μ^- divided by the sum, as described by $(\mu^+ - \mu^-)/(\mu^+ + \mu^-)$, where μ^+ and μ^- denote XAS obtained from right-hand circular polarized (RCP) and left-hand circular polarized (LCP) x-rays, respectively. (a)-(f) XMCD at $T = 83, 109, 160, 208, 254,$ and 300 K, respectively. We observe the typical XMCD signals at low temperatures and a finite XMCD signal at ambient temperature, suggesting that the SL remains ferromagnetic at 300 K. The magnitude of magnetization at different temperatures can be quantitatively estimated using spin sum rule. The orbital (L) and spin (S) contributions can be calculated using the following equations [S10],

$$M_{orbital} = -\frac{4 \int_{L_3+L_2} (\mu^+ - \mu^-) d\omega}{3 \int_{L_3+L_2} (\mu^+ + \mu^-) d\omega} (10 - n_{3d}) \dots \dots \dots (1)$$

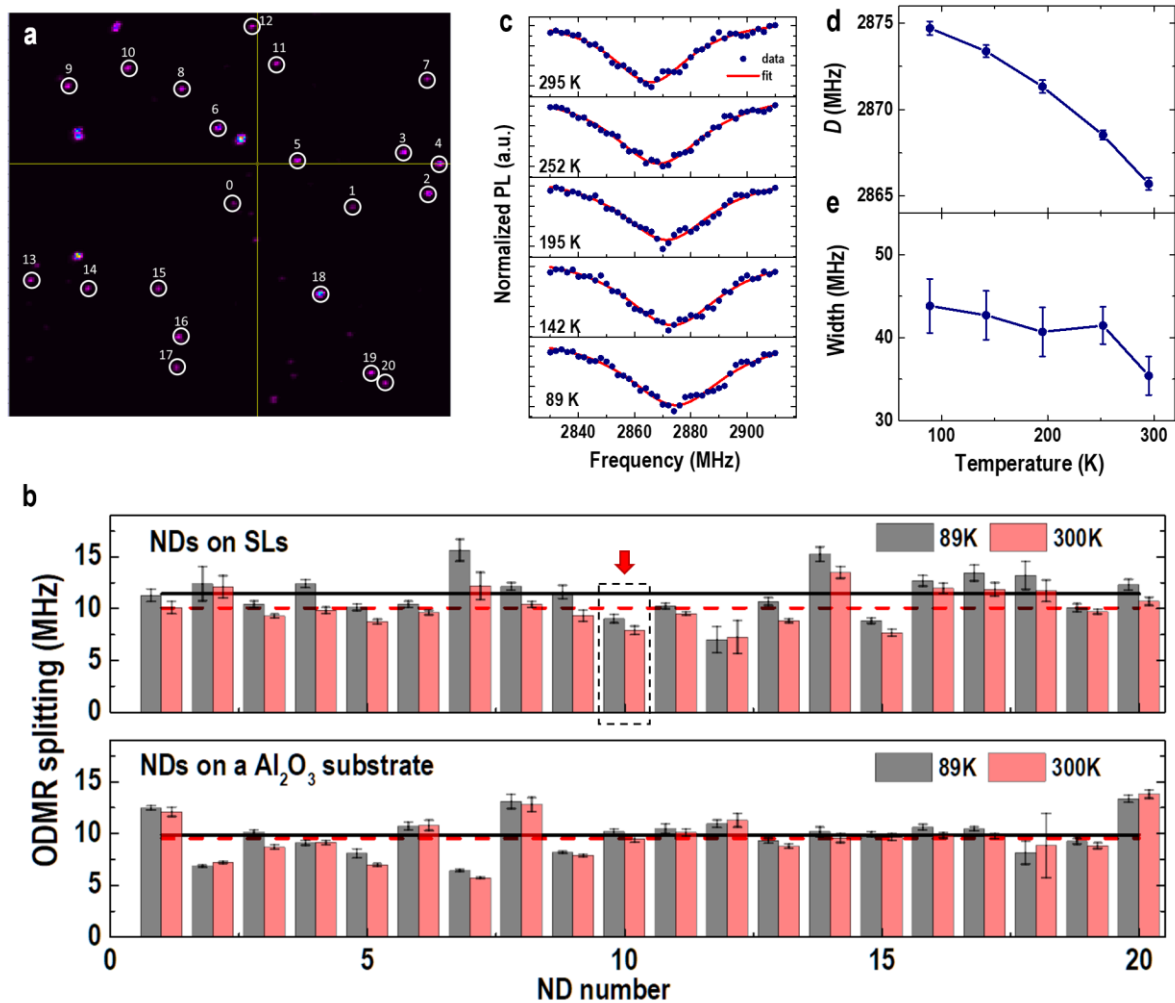
$$M_{spin} = -\frac{6 \int_{L_3} (\mu^+ - \mu^-) d\omega - 4 \int_{L_3+L_2} (\mu^+ - \mu^-) d\omega}{\int_{L_3+L_2} (\mu^+ + \mu^-) d\omega} (10 - n_{3d}) \left(1 + \frac{7 \langle T_Z \rangle}{2 \langle S_Z \rangle}\right)^{-1} \dots (2)$$

Where n_{3d} is the number of 3d electron per cations (3 for Cr ions in our work), $\langle T_Z \rangle$ is the expectation value of the magnetic dipole operator and $\langle S_Z \rangle$ is the value of in Hartree atomic

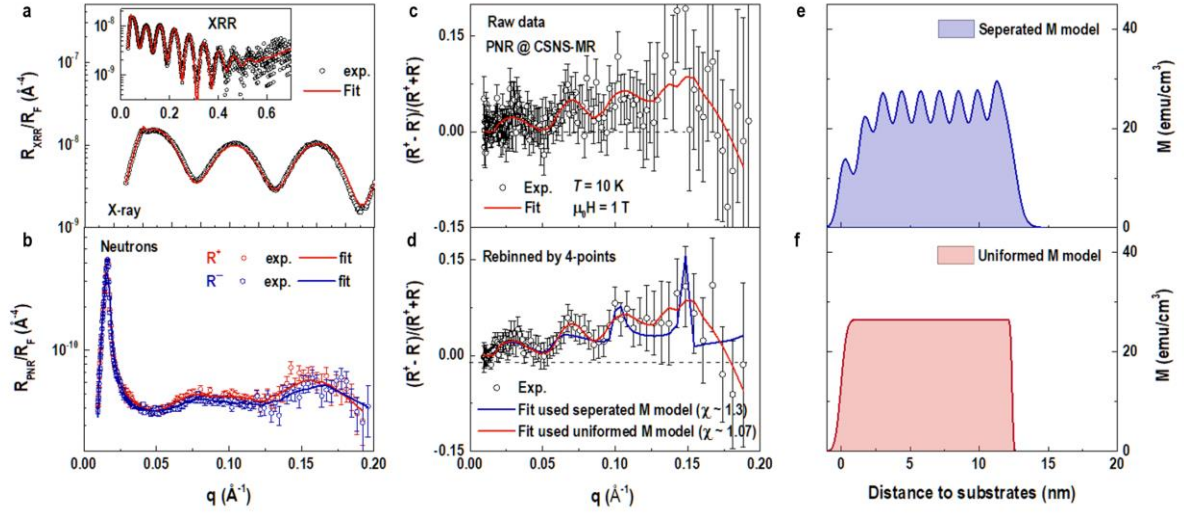
units, which could be omitted during the calculation, since the contribution of $\frac{7\langle T_Z \rangle}{2\langle S_Z \rangle}$ is very small.

Therefore, we ignore $(1 + \frac{7\langle T_Z \rangle}{2\langle S_Z \rangle})^{-1}$ in the calculations. The calculations are straightforward.

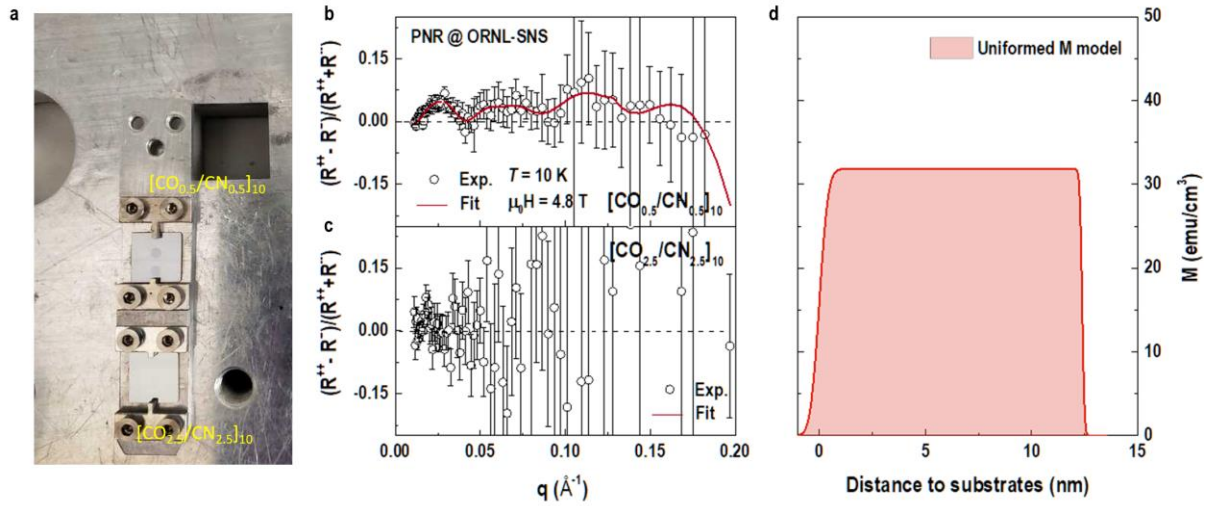
(g) XAS spectra and integrations for Cr *L*-edges at 86 K. XAS is subtract background using step function. (h) XMCD spectra and integrations for Cr *L*-edges at 86 K. Taking the integration and putting the n_{3d} numbers back to Equations (1) and (2), the spin and orbital moments of Cr ions are determined to be 0.1 and 0.03 μ_B/Cr , respectively. (i) Calculated spin (*S*), orbital (*L*) and total moments (*M*) of Cr ions at different temperatures. We conclude here that the XMCD results imply that there is parallel or near-parallel alignment of the Cr spins, possibly due to the onset of ferromagnetism or canted antiferromagnetism at the interfaces. The trend of *M* as a function of temperature is in good agreement with the SQUID magnetometry results.



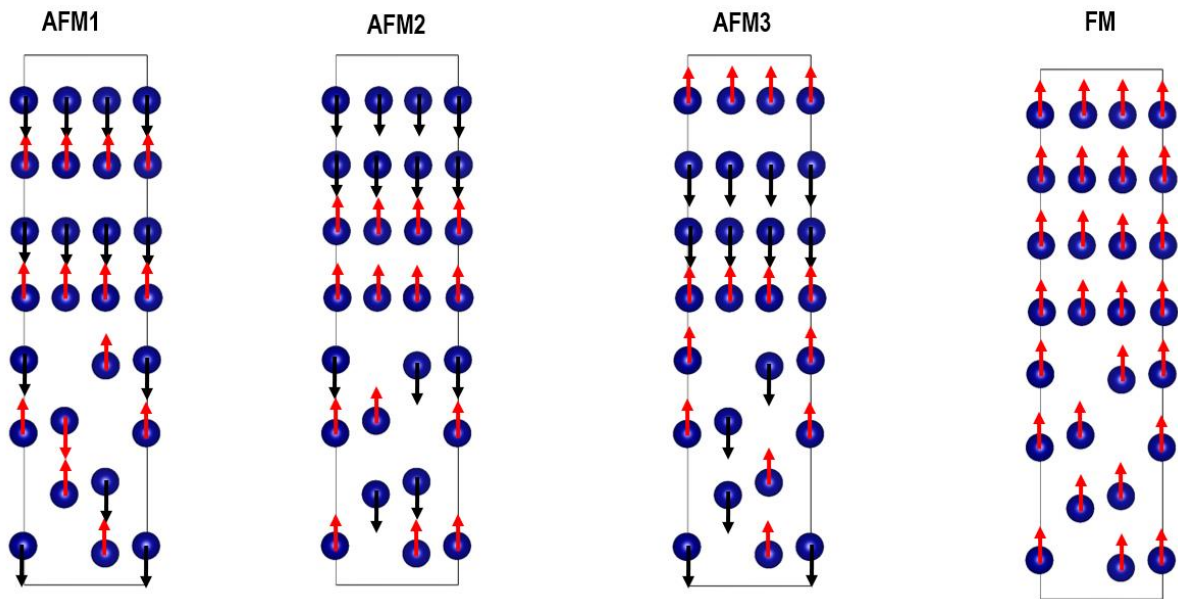
Supplementary Fig. S10. Diamond NV-based magnetometry on a [CO_{0.5}/CN_{0.5}]₁₀ superlattice. (a) Confocal image of nanodiamonds (NDs) on a Cr₂O₃/CrN SL. The bright spots are dispersive NDs. The scanning range of this image is about 20×20 μm². (b) Statistic results of ODMR splitting at 89 K and 300 K. The up panel shows ODMR splitting of NDs on the SLs, with average values of 11.4 MHz at 89 K (black line) and 10.1 MHz at 300 K (red dash line), respectively. The bottom panel shows ODMR splitting of NDs on a bare Al₂O₃ substrate, which shows nearly no temperature dependence. (c) ODMR spectra of ND₀ at various temperatures. Red lines are Lorentz single-peak fittings. (d) Zero-filed splitting, *D*, and (e) ODMR width of ND₀ as function of temperature. For this single ND, the gradient of the stray field from the SLs is so large that there is no two-peak feature in the ODMR spectra. Nevertheless, the consistence in the decrease of the stray field of the SL can be seen from the decrease of the single-peak width. [S11]



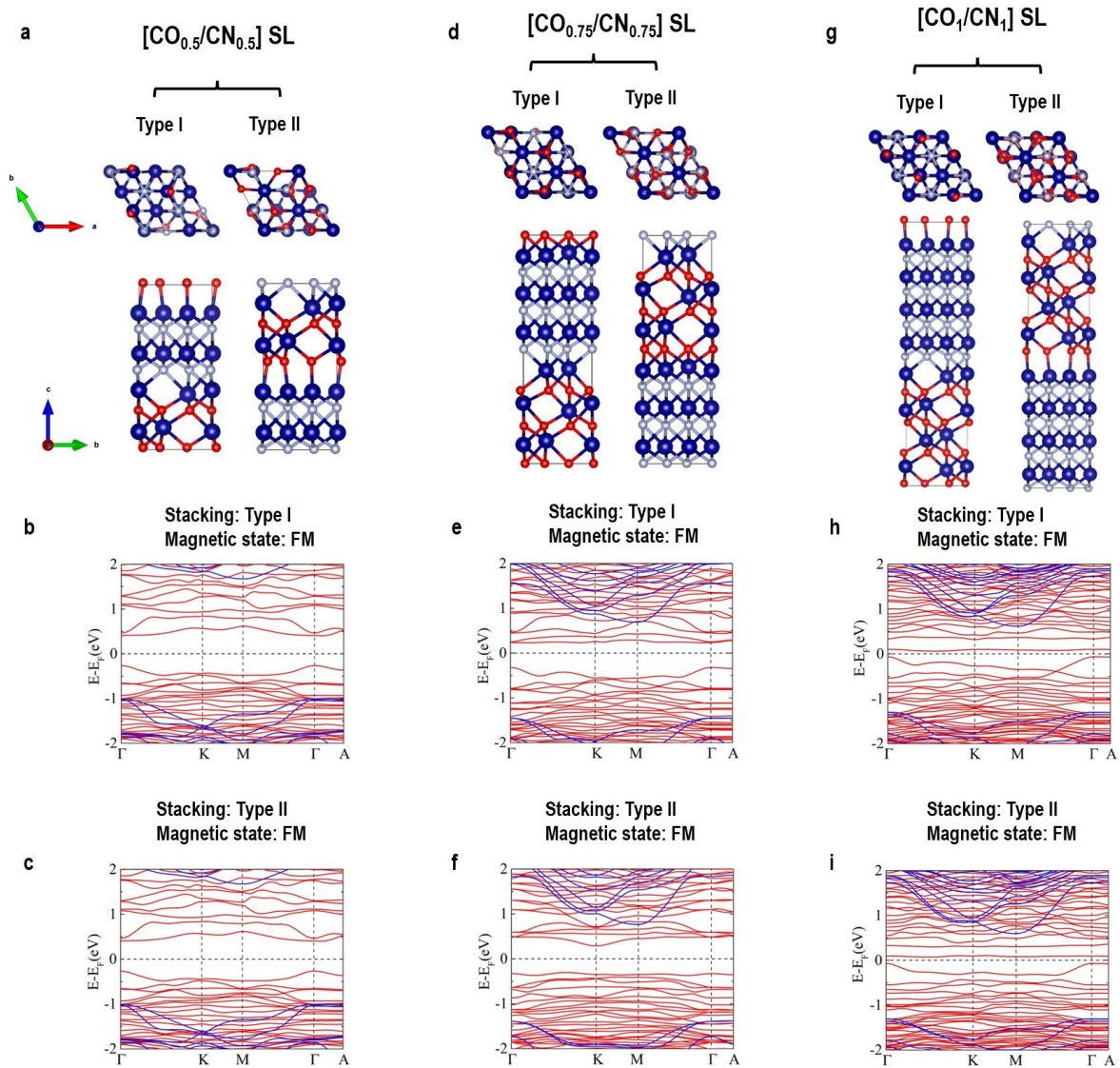
Supplementary Fig. S11. Details of PNR measurements on a $[\text{CO}_{0.5}/\text{CN}_{0.5}]_{10}$ superlattice at MR of CSNS-CAS. (a) and (b) X-ray reflectivity and neutron reflectivities of a $[\text{CO}_{0.5}/\text{CN}_{0.5}]_{10}$, respectively. Both curves are normalized to the Fresnel reflectivity $R_F (=16\pi^2/q^4)$, where q is the wave vector transfer. PNR measurements were taken at 10 K after field cooling in 1 T. Open circles and solid lines are the experimental data and best fits to the reflectivities, respectively. Inset of (a) shows the full data set and fit to the XRR. (c) Spin asymmetry (open circles) calculated as $(R^+ - R^-)/(R^+ + R^-)$, and its corresponding fit (solid line) are plotted as a function of \vec{q} . These data are the raw dataset. Rebinned SA and corresponding fits are plotted in (d). Rebinned data is refined by combining nearest 4 data points and calculating their corresponding error bars. Both data represent the same physical meaning, however, the rebinned data have smaller error bars and clearer trend. We fit the PNR data with two different models. One is a model with the separated magnetization in the CrN and Cr_2O_3 layers, as shown in the blue curve in (d) and magnetization depth profile in (e). Another is a model same as its chemical profile derived from XRR (shown in Fig. S2a) and is used for fitting the neutron reflectivities, as shown in the red curve in (d) and magnetization depth profile in (f). We obtain a smaller figure of merit ($\chi \sim 1.07$) in the uniform magnetization model than that ($\chi \sim 1.3$) in the separated magnetization model. We believe that the PNR results in this work are not sufficient to separate the magnetization contribution in the CrN and Cr_2O_3 layers with a thickness of 0.5 nm, given that the PNR measurements only extended to $\sim 0.2 \text{ \AA}^{-1}$. Therefore, the averaged magnetization of a $[\text{CO}_{0.5}/\text{CN}_{0.5}]_{10}$ superlattice is $\sim 26.5 \pm 5.0 \text{ emu/cm}^3$, in agreement with our SQUID result. PNR measurements used here are strong evidence for the existing in-plane net moment in the $[\text{CO}_{0.5}/\text{CN}_{0.5}]_{10}$ superlattice under the magnetic fields.



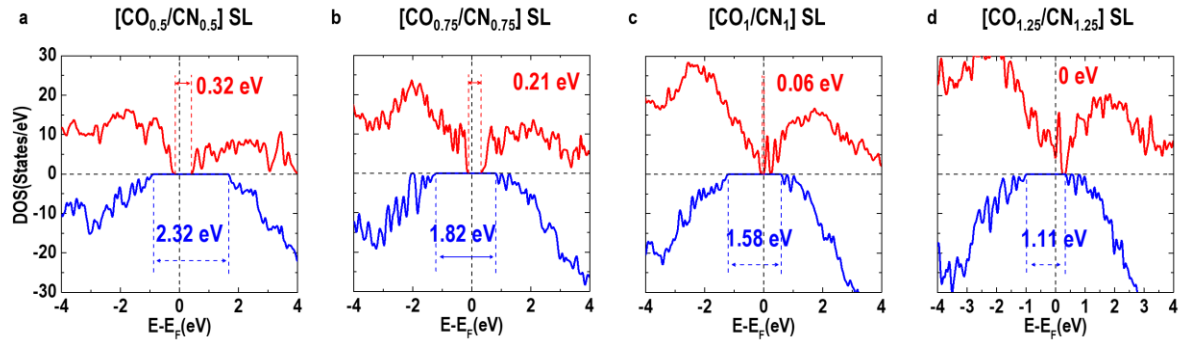
Supplementary Fig. S12. Simultaneous PNR measurements on a $[\text{CO}_{0.5}/\text{CN}_{0.5}]_{10}$ and a $[\text{CO}_{2.5}/\text{CN}_{2.5}]_{10}$ superlattice at BL4A of SNS-ORNL. (a) Sample geometry and measuring setup. Samples were aligned perpendicularly to the reflection plane and were field cooled in 4.8 T to 10 K. The neutron reflectivities were taken simultaneously from a $[\text{CO}_{0.5}/\text{CN}_{0.5}]_{10}$ (top) and a $[\text{CO}_{2.5}/\text{CN}_{2.5}]_{10}$ (bottom) superlattice in a single measurement. This type of measurement uniquely helps us to directly compare the magnetization from two samples excluding the artifacts from the instrumental errors or neutron polarization ratio. (b) and (c) Spin asymmetry (SA) and its corresponding fit as a function of \vec{q} for $[\text{CO}_{0.5}/\text{CN}_{0.5}]_{10}$ and $[\text{CO}_{2.5}/\text{CN}_{2.5}]_{10}$, respectively. The $[\text{CO}_{0.5}/\text{CN}_{0.5}]_{10}$ shows a clear SA, whereas the SA of $[\text{CO}_{2.5}/\text{CN}_{2.5}]_{10}$ is indistinguishable from the noise level. These results are in a good agreement with SQUID results that a $[\text{CO}_{0.5}/\text{CN}_{0.5}]_{10}$ sample has a significant higher magnetization than that of $[\text{CO}_{2.5}/\text{CN}_{2.5}]_{10}$. (d) Magnetization depth profile of $[\text{CO}_{0.5}/\text{CN}_{0.5}]_{10}$ under a field of 4.8 T at 10 K. Similarly, we determine that the average magnetization of $[\text{CO}_{0.5}/\text{CN}_{0.5}]_{10}$ superlattice is $31.8 \pm 7.0 \text{ emu}/\text{cm}^3$ at 4.8 T, which is close to that of $[\text{CO}_{0.5}/\text{CN}_{0.5}]_{10}$ ($26.5 \pm 5.0 \text{ emu}/\text{cm}^3$) at 1 T. We believe that the magnetization of $[\text{CO}_{0.5}/\text{CN}_{0.5}]_{10}$ is close to saturation when the magnetic field is beyond 1 T. These results confirm: 1) the average ferromagnetism in the $\text{Cr}_2\text{O}_3/\text{CrN}$ superlattices decays with increasing layer thickness, 2) the PNR measurements repeatedly assert the net magnetization in the $[\text{CO}_{0.5}/\text{CN}_{0.5}]_{10}$ superlattice.



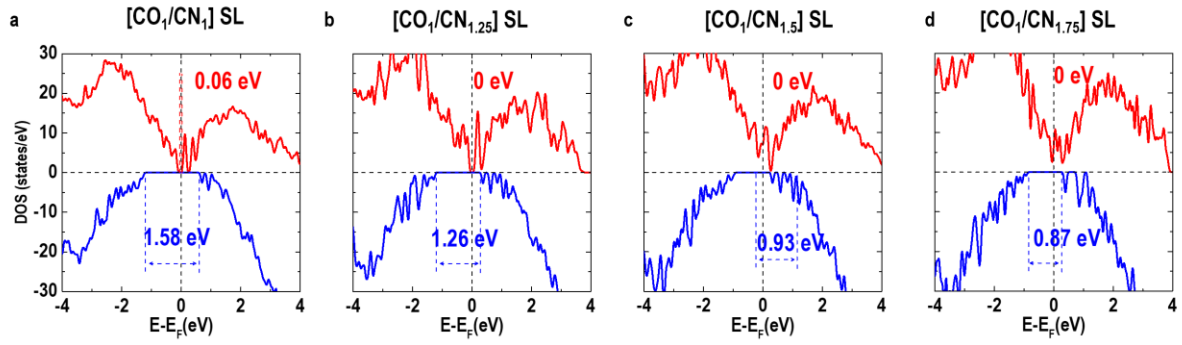
Supplementary Fig. S13. Magnetic states tested in $\text{Cr}_2\text{O}_3/\text{CrN}$ superlattices. Without distortions, bulk Cr_2O_3 is an antiferromagnetic (AFM) insulator. Taken $[\text{CO}_1/\text{CN}_1]$ slab as an example, under relatively small lattice distortion due to the lattice mismatch between CrN and Cr_2O_3 as well as substrate-induced epitaxial strain, three different AFM configurations may appear. [S12] We have tested three different initial AFM states for the superlattices and found that the ground state is FM in the superlattices with different layer thicknesses.



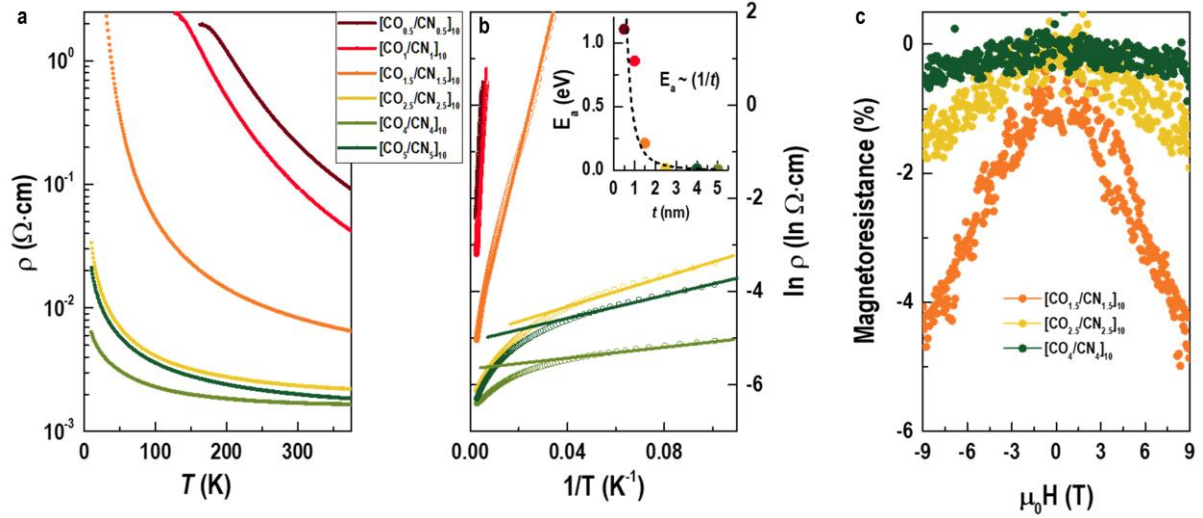
Supplementary Fig. S14. Diagrams of the crystal structures and band structures of $\text{Cr}_2\text{O}_3/\text{CrN}$ superlattices. Top-view and side-view of the superlattices with two different types of stacking orders for (a) $[\text{CO}_{0.5}/\text{CN}_{0.5}]$, (d) $[\text{CO}_{0.75}/\text{CN}_{0.75}]$, (g) $[\text{CO}_1/\text{CN}_1]$ slabs. The blue, red, and silver balls represent the Cr, O, and N atoms, respectively. (b)-(c) Band structures for (b, c) $[\text{CO}_{0.5}/\text{CN}_{0.5}]$, (e, f) $[\text{CO}_{0.75}/\text{CN}_{0.75}]$, and (h, i) $[\text{CO}_1/\text{CN}_1]$ slabs with stacking types I and II. Red and blue curves represent the spin-up and spin-down bands, respectively. All of these band structures exhibit ferromagnetic ground states. Apparently, the bandgap reduces with increasing the CO (CN) layers thickness, suggesting that the conductances of these superlattices increase accordingly.



Supplementary Fig. S15. Diagrams of the density of states (DOS) for $[\text{CO}_t/\text{CN}_t]$ slabs with symmetric layer thicknesses. (a) $[\text{CO}_{0.5}/\text{CN}_{0.5}]$, (b) $[\text{CO}_{0.75}/\text{CN}_{0.75}]$, (c) $[\text{CO}_1/\text{CN}_1]$, and (d) $[\text{CO}_{1.25}/\text{CN}_{1.25}]$ slabs with stacking types I, respectively. The red and blue lines represent the spin-up and spin-down channels, respectively. The bandgaps for spin-up and spin-down channels are noted in each figure. As increasing the layer thickness, the bandgaps in both spin-up and spin-down channels reduce. For the $[\text{CO}_{1.25}/\text{CN}_{1.25}]$ slabs, the spin-up channel exhibits a bandgap closure.



Supplementary Fig. S16. Diagrams of the density of states (DOS) for $[\text{CO}_1/\text{CN}_t]$ slabs with different CrN layer thicknesses. (a) $[\text{CO}_1/\text{CN}_1]$, (b) $[\text{CO}_1/\text{CN}_{1.25}]$, (c) $[\text{CO}_1/\text{CN}_{1.5}]$, and (d) $[\text{CO}_1/\text{CN}_{1.75}]$ slabs with stacking types I, respectively. We keep the CO layer thickness as a constant and gradually increase the conducting CrN layer thickness. The bandgaps for spin-up channels close and the bandgaps for spin-down channels reduce significantly. Thus, the trend of bandgap closure is consistent with that of $[\text{CO}_t/\text{CN}_t]$ slabs with symmetric layer thickness.



Supplementary Fig. S17. Transport property of Cr₂O₃/CrN superlattices. All Cr₂O₃/CrN superlattices exhibit insulating behavior. The resistivity drops with increasing Cr₂O₃ (CrN) layer thickness. We estimated the thermal activation energy (E_a) of charge carriers in Cr₂O₃/CrN superlattices by linearly fitting the $\ln(\rho)$ - T^{-1} curves, as shown in (b). The inset in (b) shows E_a as a function of layer thickness. For $[\text{CO}_{0.5}/\text{CN}_{0.5}]_{10}$, E_a is 1.1 eV. E_a decreases with increasing layer thickness, following the $E_a \sim t^{-1}$. For $[\text{CO}_5/\text{CN}_5]_{10}$, E_a is only 6.7 meV. The thickness dependence of the resistivity and thermal activation energy are in good agreement with the theoretical calculations. The thicker Cr₂O₃/CrN superlattices exhibit greater conductivity. (c) Magnetoresistance (MR) as a function of field for $[\text{CO}_t/\text{CN}_t]_{10}$ ($t = 1.5, 2.5$, and 4 nm) superlattices. The resistivities of $[\text{CO}_t/\text{CN}_t]_{10}$ ($t < 1.5$) is too high to be measured at 10 K. The highest MR at 9 T is $\sim 4.5\%$ for $[\text{CO}_{1.5}/\text{CN}_{1.5}]_{10}$. MR decays as increasing the layer thickness, suggesting the decrease of magnetization, in excellent agreement with our magnetization measurements.

Sample	Type	AFM1 (eV)	AFM2 (eV)	AFM3 (eV)	FM (eV)
[CO _{0.5} /CN _{0.5}] SL	Type I	-172.468	-172.619	-172.542	-173.208
	Type II	-172.531	-172.718	-172.345	-173.206
[CO _{0.75} /CN _{0.75}] SL	Type I	-262.275	-262.340	-260.787	-262.808
	Type II	-262.220	-262.321	-262.049	-262.638
[CO ₁ /CN ₁] SL	Type I	-347.127	-347.573	-347.127	-350.374
	Type II	-347.111	-347.494	-347.913	-349.848

Supplementary Table S1. Comparison of calculated energies for the Cr₂O₃/CrN superlattices with different magnetic configurations. The energies of the ferromagnetic (FM) ground states for all SLs are the lowest (marked in red), independent of stacking orders. The calculation results suggest that the most stable magnetic ground state for Cr₂O₃/CrN superlattices is the FM state, consistent with our experimental observations.

Sample	Type	Bandgap (meV)	Cr (μ_B)	O (μ_B)	N (μ_B)	Total net moment (μ_B)
[CO _{0.5} /CN _{0.5}] SL	Type I	667	3.102	-0.075	-0.230	29.196
	Type II	658	3.103	-0.072	-0.235	29.192
[CO _{0.75} /CN _{0.75}] SL	Type I	552	3.056	-0.066	-0.163	43.781
	Type II	594	3.057	-0.066	-0.163	43.781
[CO ₁ /CN ₁] SL	Type I	146	3.059	-0.064	-0.175	58.377
	Type II	124	3.060	-0.064	-0.175	58.377

Supplementary Table S2. Calculated bandgap, magnetic moments for each element, and total net moment of the Cr₂O₃/CrN superlattices. The bandgap decreases with increasing layer thickness, indicating that the conductance should be higher for the thick superlattices. This conductivity trend is understandable because bulk CrN is an antiferromagnetic metal with an ultralow resistivity ($\sim 10^{-4} \Omega \cdot \text{cm}$ at the room temperature). Our previous work demonstrated that (111)-oriented CrN films undergo a metal-to-insulator transition (MIT) below 100 u.c. [S8, S9] due to the substrate induced compressive strain. We believe that the MIT may happen in the superlattices as well. If the thickness of CrN interlayers increases beyond 100 u.c., the superlattices should eventually become metallic. We calculated the total net magnetic moments of the superlattices as well. Although the total moment increases with layer thickness, the average magnetic moment for the superlattices decreases, consistent with our experimental results. These results suggest that the magnetic net moment arises from ferromagnetic exchange coupling across the interface.

Supplementary reference

- [S1]. Björck, M. & Andersson, G. GenX: an extensible X-ray reflectivity refinement program utilizing differential evolution. *J. Appl. Cryst.* **40**, 1174-1178 (2007).
- [S2]. Zhang, K. H. L. *et al.* Electronic and magnetic properties of epitaxial perovskite SrCrO₃(001). *J. Phys.: Condens. Matter* **27**, 245605 (2015).
- [S3]. Qiao, L. *et al.* The impact of crystal symmetry on the electronic structure and functional properties of complex lanthanum chromium oxides. *J. Mater. Chem. C* **1**, 4527-4535 (2013).
- [S4]. Nichols, J. *et al.* Emerging magnetism and anomalous Hall effect in iridate–manganite heterostructures. *Nat. Commun.* **7**, 12727 (2016).
- [S5]. Guo, E. -J. *et al.* Spatially Resolved Large Magnetization in Ultrathin BiFeO₃. *Adv. Mater.* **29**, 1700790 (2017).
- [S6]. Li, S. *et al.* Strong ferromagnetism achieved via breathing lattices in atomically thin cobaltites. *Adv. Mater.* **33**, 2001324 (2021).
- [S7]. Yi, D. *et al.* Emergent electric field control of phase transformation in oxide superlattices. *Nat. Commun.* **11**, 902 (2020).
- [S8]. Jin, Q. *et al.* Strain-mediated high conductivity in ultrathin antiferromagnetic metallic nitrides. *Adv. Mater.* **33**, 2005920 (2021).
- [S9]. Jin, Q. *et al.* Structural twinning induced insulating phase in CrN (111) films. *Phys. Rev. Mater.* **5**, 023604 (2021).
- [S10]. C. T. Chen *et al.*, *Phys. Rev. Lett.* **75**, 152 (1995).
- [S11]. Acosta, V. M. *et al.* Temperature Dependence of the Nitrogen-Vacancy Magnetic Resonance in Diamond. *Phys. Rev. Lett.* **104**, 070801 (2010).
- [S12]. Maldonado, F., Rivera, R. & Stashans, A. Structure, electronic and magnetic properties of Ca-doped chromium oxide studied by the DFT method. *Physica B* **407**, 1262–1267 (2012).